Article

Radiative forcing from aerosol–cloud interactions enhanced by large-scale circulation adjustments

Guy Dagan [1] ✉, Netta Yeheskel[1] & Andrew I. L. Williams[2]

The impact of anthropogenic aerosols on clouds is a leading source of uncertainty in estimating the effect of human activity on the climate system. The challenge lies in the scale difference between clouds (~1–10 km) and general circulation and climate (>1,000 km). To address this, we use convection-permitting simulations conducted in a long and narrow domain, to resolve convection while also including a representation of large-scale processes. We examine a set of simulations that include a sea surface temperature gradient—which drives large-scale circulation—and compare these with simulations that include no gradient. We show that the effective radiative forcing due to aerosol–cloud interactions is strongly enhanced by adjustments of large-scale circulation to aerosol. We find that an increase in aerosol concentration suppresses precipitation in shallow-convective regions, which enhances water vapour transport to the portion of the domain dominated by deep convection. The subsequent increase in latent heat release in deep-convective regions strengthens the overturning circulation and surface evaporation. These changes can explain the increase in cloudiness under higher aerosol concentrations and, consequently, the large aerosol radiative effect. This work highlights the fundamental importance of large-scale circulation adjustments in understanding the effective radiative forcing from aerosol–cloud interactions.

Human activity can create an imbalance in the Earth's radiation budget known as radiative forcing. One of the most substantial drivers of radiative forcing, in addition to greenhouse gases, are aerosols[1]. An increase in aerosol concentration, capable of serving as cloud condensation nuclei (CCN) for the formation of cloud droplets, generally results in smaller but more numerous droplets and an instantaneous change in the radiative properties of the clouds[2,3]. Furthermore, this initial perturbation can result in cloud 'adjustments', which can affect the amount of clouds or their total water content[4]. Adjustments refer to changes in the system's state or composition, including large-scale circulation changes, that modify the initial energy imbalance without surface temperature changes[5]. The sum of the immediate cloud response

and subsequent cloud adjustment's impact on the top-of-atmosphere (TOA) radiation balance is known as the effective radiative forcing from aerosol–cloud interactions (ERF_{ACI})[1,6].

Uncertainties in ERF_{ACI} are a key source of climate change understanding uncertainty[7]. These uncertainties arise primarily owing to cloud adjustments[1], which are difficult to constrain causally through observations[8]. On the other hand, studying ACI in numerical models allows one to better understand physical processes, but the high spatio-temporal resolution required to capture ACI makes it difficult to simulate the feedbacks of local ACI with the global atmospheric circulation. This is problematic because large-scale circulation adjustments are known to play a robust role in the ERF from CO_2 (ref. 9) and

[1]Fredy and Nadine Herrmann Institute of Earth Sciences, Hebrew University, Jerusalem, Israel. [2]Program in Atmosphere and Ocean Sciences, Princeton University, Princeton, NJ, USA. ✉e-mail: guy.dagan@mail.huji.ac.il
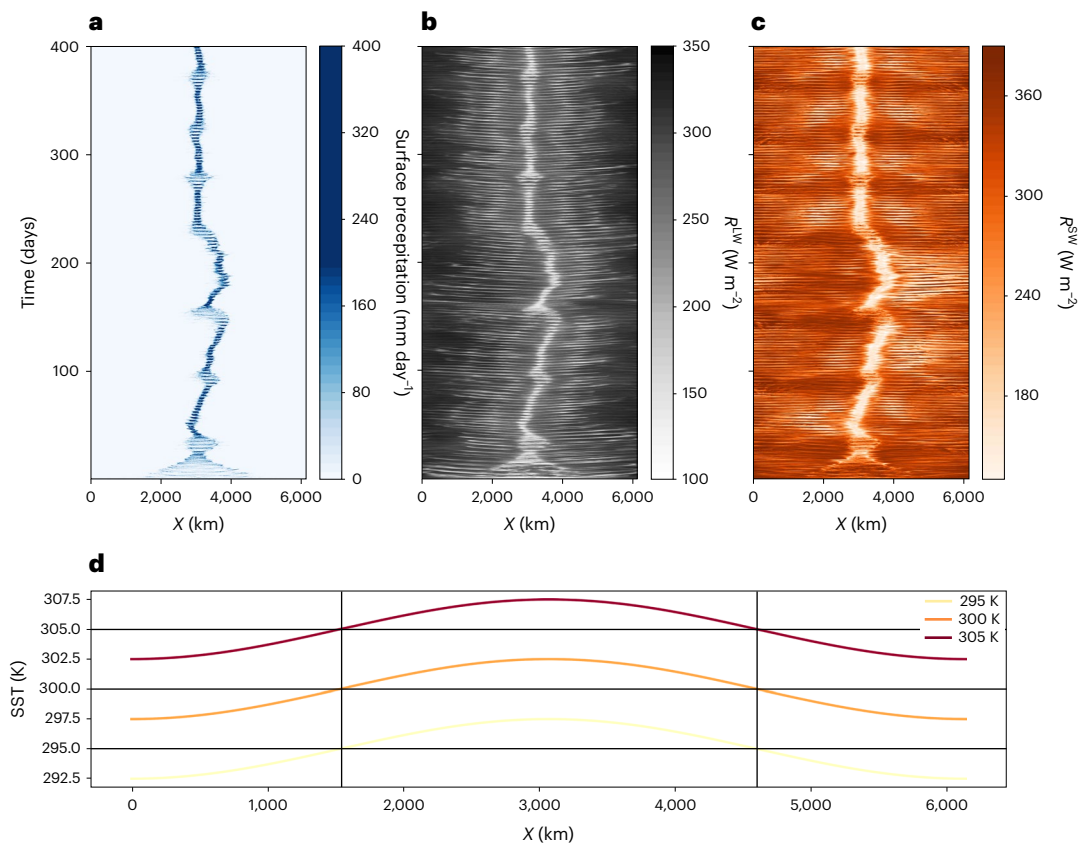
Fig. 1 | Mock-Walker simulations. a–c, Hovmöller diagrams showing the spatio-temporal distribution of key variables in the mock-Walker simulations: surface precipitation (**a**), TOA outgoing longwave radiation (R^{LW}) (**b**) and TOA net shortwave radiation (R^{SW}) (**c**). **d**, The SST distributions along the long dimension (X) of the domain of the mock-Walker simulations, with black vertical lines indicating the boundary between the shallow- and deep-convective regimes (see Methods for details). **a–c** correspond to simulations with a domain-mean SST of 300 K and N_a of 200 cm^{-3}.

from aerosol–radiation interactions[10]. Nevertheless, the importance of circulation adjustments for ACI (the indirect effect), which is subject to a much greater scale imbalance owing to the need to resolve microphysical processes, is not yet clear. This represents a critical knowledge gap in our understanding of how anthropogenic aerosols affect Earth's climate. More generally, better understanding of the coupling between clouds and large-scale circulations has been identified as one of climate science's 'grand challenges'[11], highlighting the need for further research in this area (for observational estimates of this coupling in our region of interest, the tropical Pacific, see Supplementary Discussion 1).

In recent years, cloud-resolving simulations using long-channel domains have arisen as a potential solution to the scale mismatch between the small scale of clouds and the much larger scale of the climate and general circulation[12–16]. By employing a long, narrow channel domain geometry, this setup accounts for the large scale of the tropical climate system while still allowing for high temporal and spatial resolutions, as only one horizontal dimension is fully considered. Such a geometry can be used with either horizontal homogeneous sea surface temperature (SST) conditions[14] or with an SST gradient that produces a large-scale circulation resembling the Walker circulation[16]. The latter approach is referred to as a mock-Walker simulation[17,18]. This approach has been used to understand convective aggregation and cloud feedbacks, but has not yet been used to study ACI and potential large-scale circulation adjustments.

In this Article, we investigate ACI in simulations that account for large-scale circulation (long-channel domain) and under equilibrium conditions (long radiative–convective equilibrium (long RCE) simulations[14,19]). We examine simulations conducted with the System for

Atmospheric Modeling (SAM[20]) with an SST gradient-forced circulation (mock-Walker simulations; Fig. 1), across different domain-mean SSTs (Methods).

Sensitivity of radiation and clouds to aerosol concentration

We first examine the TOA radiative effect of an increase in aerosol concentration (N_a; Fig. 2). As expected, it demonstrates that an increase in N_a drives a negative TOA energy gain (ΔR; Fig. 2a). Most of the ΔR response can be explained by a reduction in the net TOA shortwave energy gain (ΔR^{SW}; Fig. 2b), with only a minor effect in the longwave (ΔR^{LW}; Fig. 2c). In addition, this figure demonstrates that ΔR is driven by changes in the cloud radiative effect (ΔCRE; Methods; for example, see the resemblance between Fig. 2a–c and 2d–f). The negative trend in R^{SW} with N_a has roughly equal contributions from the shallow and deep parts of the domain (divided into warmer and colder than the average SST; Supplementary Fig. 3). We note that the radiative effects are roughly logarithmic with N_a (Fig. 2).

Our estimate of $\frac{\partial R}{\partial \ln N_a}$, which accounts for large-scale circulation adjustments, is higher than recent estimates based on observations which focus on the local response[21]. Specifically, Wall et al.[21] evaluated $\frac{\partial R}{\partial \ln N_d}$ to be around −7 W m^{-2} for marine liquid-only clouds over the global ocean (where N_d is the cloud droplet number concentration). In our case, on the basis of the average over the different SSTs and N_a considered here, $\frac{\partial R}{\partial \ln N_a}$ is estimated to be −9.2 W m^{-2} (the full range of estimations being −5.5 to −15.3 W m^{-2}). While this comparison should be taken cautiously owing to multiple differences in the focus and analysis methods (for example, focusing only on liquid clouds in ref. 21 versus focusing also on deep clouds here, the use of N_d versus N_a
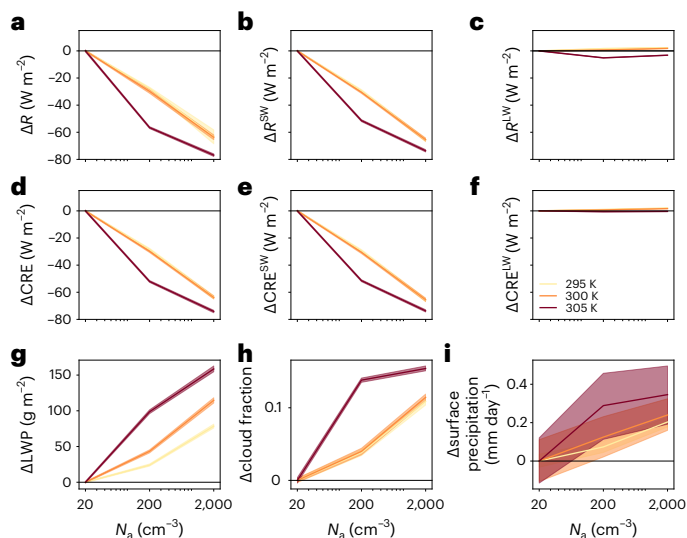
Fig. 2 | Radiative and cloud property response. a–c, The change in the net TOA energy gain (ΔR) in total (shortwave + longwave) (**a**), in the shortwave (**b**) and in the longwave (**c**). **d–f**, The change in the CRE in total (shortwave + longwave) (**d**), in the shortwave (**e**) and in the longwave (**f**). **g–i**, The change in the domain-mean (including clear sky areas) LWP (**g**), CF (**h**) and surface precipitation (**i**) owing to a change in aerosol concentration N_a (compared with the cleanest case of 20 cm^{-3}), for different SSTs (indicated by different curves). Solid lines represents domain-mean values, while shaded areas represent the 95th percentile uncertainty intervals (n = 7,200).

and the averaging over the global ocean versus the focus only on the tropics), it still suggests the possibility that large-scale circulation adjustments amplify the sensitivity of TOA fluxes to changes in aerosol concentration. For example, we note that, in the same model and using a similar setup but without an SST gradient (and hence no representation of forced large-scale overturning circulation), $\frac{\partial R}{\partial \ln N_a}$ is an order of magnitude smaller than in the presence of large-scale circulation (Supplementary Fig. 4). However, this comparison is complicated by differences in the distribution of cloud types between the two control simulations.

The positive N_a-driven cloud adjustments (the increases in cloud fraction (CF) and liquid water path (LWP); Fig. 2g,h) can explain the relatively strong radiative cooling effect of aerosols in these simulations. Next, we investigate where this increase in LWP and CF is coming from, that is, from the portion of the domain with warmer SSTs, which is dominated mostly by deep convection (the 'deep regime', which includes also some shallow and congestus clouds) or from the portion of the domain with colder SSTs, which is dominated by shallow clouds (the 'shallow regime'). To do this, in Fig. 3 we separate the cloud responses into these two parts of the domain. This demonstrates that the LWP and CF strongly increase in both shallow and deep parts of the domain (Fig. 3a,e and 3b,f, respectively). The cloud top height generally increases with N_a in both the shallow and deep regimes, consistent with previous studies[22–24]. Particularly important to this study, Fig. 3d,h demonstrates that the surface precipitation decreases with N_a in the shallow regime but increases in the deep regime, which overcompensates for the trend in the shallow regime and results in an overall positive trend (Fig. 2i). Figure 3 presents the results based on the simulations conducted at SST of 300 K. Supplementary Figs. 5 and 6 present the results based on the two other SSTs, which generally demonstrate consistency across different SSTs. In addition, Fig. 3 presents two methods to separate the domain into deep- and shallow-dominated regimes (Methods). These two methods generally demonstrate consistent behaviour.

Walker circulation response to aerosols

Next, we examine the sensitivity of the circulation itself to changes in N_a (Fig. 3i–p). It demonstrates that the large-scale ascent (w_{500}) is becoming stronger in the deep regime with an increase in N_a (especially in the w-based separation). Simultaneously, the near-surface wind speed is enhanced with N_a. The intensification of the magnitude of w_{500} together with the enhanced near-surface wind speed suggests that the large-scale overturning circulation strengthens with the increase in N_a. This behaviour is also seen for the other two SSTs (Supplementary Figs. 5 and 6).

The increase in near-surface wind speed is accompanied by an increase in surface evaporation in the shallow regime (Fig. 3k). This increase in surface evaporation, and the reduction in precipitation (Fig. 3d) with N_a in the shallow regime, results in stronger advection of water vapour from the shallow to the deep regimes (Fig. 4a and ref. 25). The increased water vapour convergence into the deep regime results in enhanced precipitation, stronger latent heat release and an increased export of dry static energy from the deep regime (Fig. 4b). The increase in surface evaporation and the reduction in precipitation in the shallow regime can thus explain both the local (shallow) and remote (deep) increase in precipitable water (Fig. 3l,p), and in CF and LWP, with N_a. The increase in CF and LWP with N_a, in turn, can explain the strong ΔR^{SW} response. In addition, the domain-mean increase in surface evaporation is consistent with the increase in the domain-mean precipitation (Fig. 2i), as the precipitation and evaporation must balance each other under equilibrium conditions.

Circulation adjustment increases cloudiness

On the basis of the results presented above, we propose the following process chain as an explanation for the strong ERF$_{ACI}$ in the presence of a large-scale circulation (as illustrated in Fig. 5): aerosols suppress rain in the shallow regime (Fig. 3 and item 1 in Fig. 5), which drives a stronger water vapour advection from the shallow to the deep regime (Fig. 4 and item 2 in Fig. 5). The stronger convergence of water vapour into the deep regime results in a stronger latent heat release (and hence stronger dry static energy divergence out of the deep regime; Fig. 4 and item 3 in Fig. 5), which intensifies the overturning circulation (Fig. 3 and items 4 and 5 in Fig. 5). The stronger circulation is also associated with an increase in near-surface wind speed (Fig. 3 and item 5 in Fig. 5). This, together with drying of the cloudy layer due to its deepening (Fig. 3c), precipitation suppression and the decrease in evaporation below cloud base[23,24], drives an increased surface evaporation in the shallow regime (Fig. 3k and item 6 in Fig. 5). This further intensifies the water vapour advection from the shallow to the deep regime (Fig. 4) and positively feeds back on the circulation intensification. Together, these mechanisms can explain the increase in cloudiness (LWP and CF) in both regimes, which in turn can explain the large radiative effect (Fig. 2 and item 7 in Fig. 5). We note that the surface evaporation feedback proposed here resembles the wind-induced surface heat exchange (WISHE) feedback that was proposed before for inducing convective self-aggregation[26].

To further examine the proposed process chain, and to get a qualitative estimate of the role of the WISHE feedback in our simulations compared with the local effect, we conducted a mechanism denial experiment by fixing the wind speed in the calculations of the surface fluxes in the model (Methods). By doing this, the WISHE feedback is excluded, which we expect to weaken the TOA radiative responses. Comparing the simulations with the WISHE feedback turned off (no_WISHE) and the simulations which include this feedback (Fig. 6) demonstrates that ΔR is reduced by about one-third when the WISHE effect is turned off. That is to say that the intensification of the surface fluxes owing to the increase in near-surface winds under high N_a conditions increases ERF$_{ACI}$ by about 33.3%. This trend is driven by weaker cloud adjustments in the no_WISHE simulations (Fig. 6g,h). Furthermore, the exclusion of the WISHE effect almost entirely eliminates
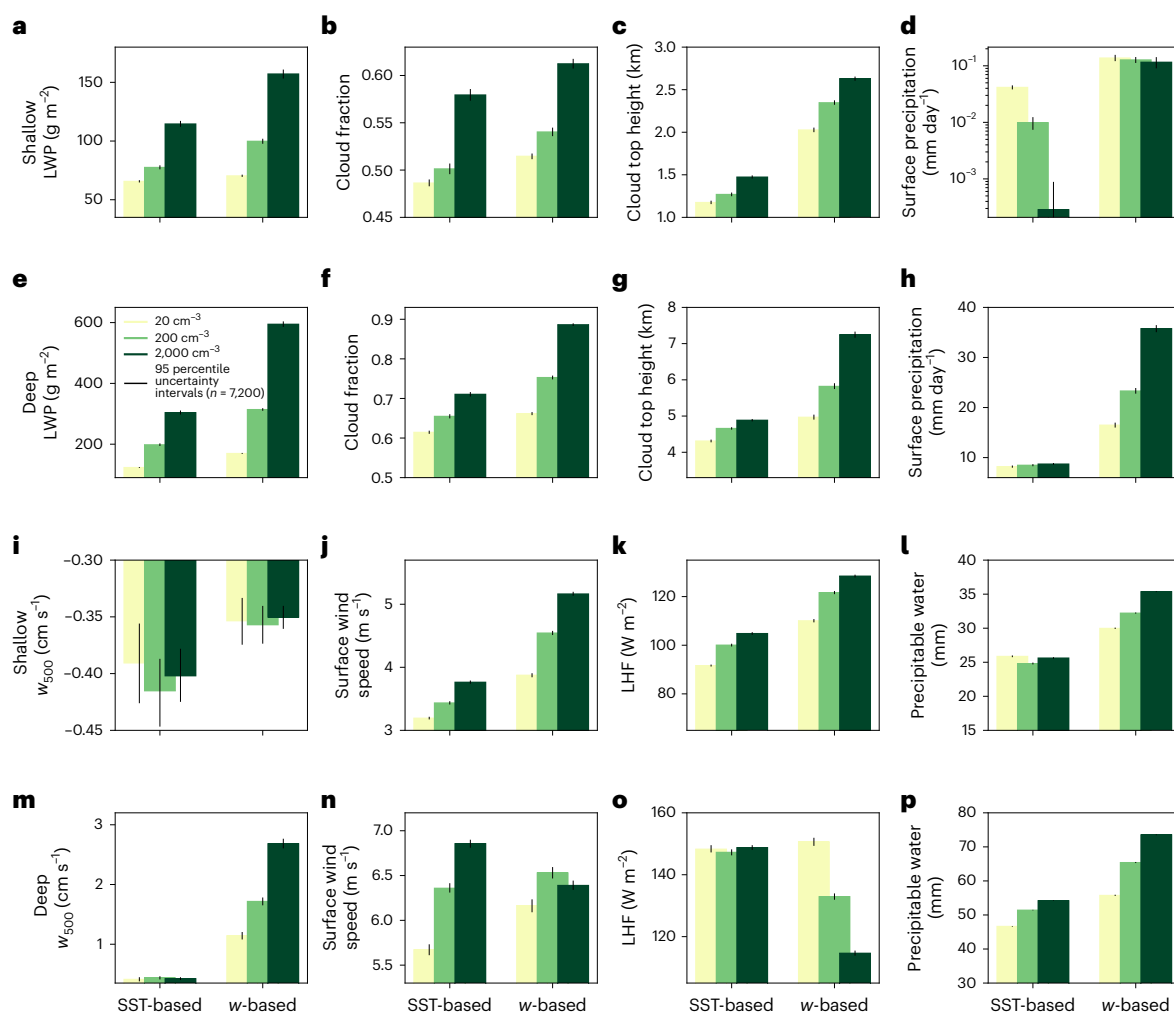
Fig. 3 | The clouds and circulation response in the different parts of the domain. a–p, The temporal and spatial mean of the LWP (including clear sky areas) (**a** and **e**), CF (**b** and **f**), cloud top height (**c** and **g**), surface precipitation (**d** and **h**), large-scale vertical velocity at 500 hPa (w_{500}, **i** and **m**), near surface wind speed (**j** and **n**), surface latent heat flux (**k** and **o**) and precipitable water (**l** and **p**) for the different mock-Walker simulations conducted with SST of 300 K and different aerosol concentrations, and for the shallow (**a–d** and **i–l**) and deep regime (**e–h** and **m–p**) separately, using two different methods for the separation (see main text for details). The bars represent the mean values, while the black vertical lines represent the 95th percentile uncertainty intervals ($n = 7,200$). Note the logarithmic scale on the y axis of **d**.

the increase in surface evaporation with N_a (Supplementary Fig. 8), which is associated also with a similarly weaker surface precipitation enhancement with N_a (Fig. 6i). Owing to the weaker increase in surface evaporation at the shallow regime with N_a in the no_WISHE simulations compared with the simulations which include this feedback, the increase in water vapour advection out of the shallow regime is also reduced (Supplementary Fig. 9).

The process chain presented above suggests that aerosol in shallow-dominated regimes, and their effect on precipitation, is key for the large-scale circulation adjustment. Another possible explanation for the ACI-driven large-scale circulation adjustment could be related to aerosol effects on deep-convective cloud. For example, it was previously proposed that an increase in N_a could affect the vertical distribution of latent heating in deep-convective clouds owing to 'convective invigoration'[27–29]. In addition, an increase in N_a could result in detainment of smaller and more numerous ice crystals into anvil clouds[30,31], which could change the net atmospheric radiative heating rates. Both of these effects could change the vertical distribution of diabatic heating in convective regions, which could affect the Walker circulation[32]. Hence, to examine the relative role of aerosol
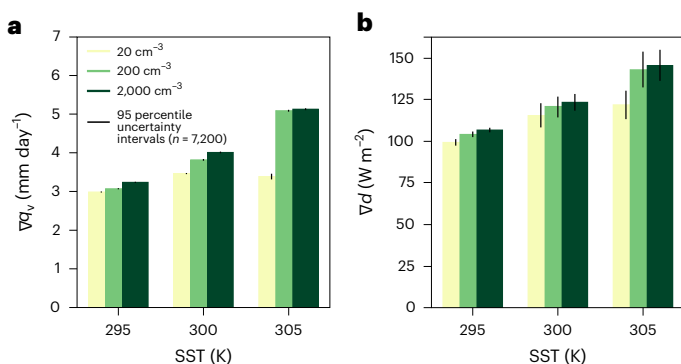

Fig. 4 | The water vapour and dry static energy divergence response. a,b, The mean water vapour divergence (∇q_v) out of the shallow regime (**a**) and the mean dry static energy divergence out of the deep regime (∇d, **b**) for different mock-Walker simulations conducted with different SSTs and aerosol concentrations using the SST-based separation (see main text for details). Bars represent mean values, while vertical black lines represent the 95th percentile uncertainty intervals ($n = 7,200$). Supplementary Fig. 7 presents the same results but for the w-based separation for the shallow and deep parts.
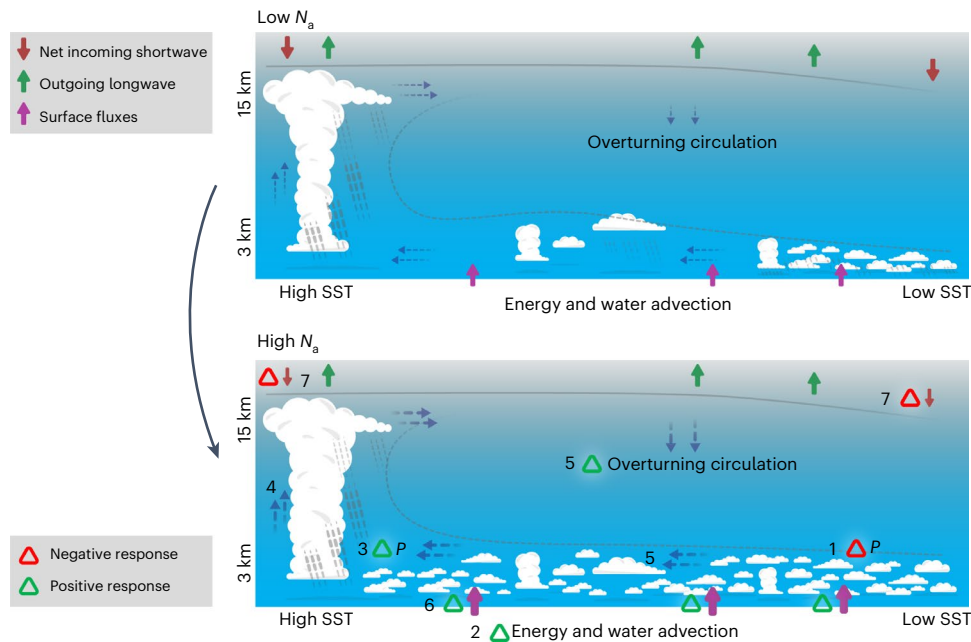
Fig. 5 | Cloud–circulation coupling. A schematic representation of the coupling between clouds and circulation in the tropics under clean conditions (top) and the response of this coupled system to an increase in aerosol concentration (bottom). The solid and dashed lines represent the tropopause and the subsiding inversion, respectively.
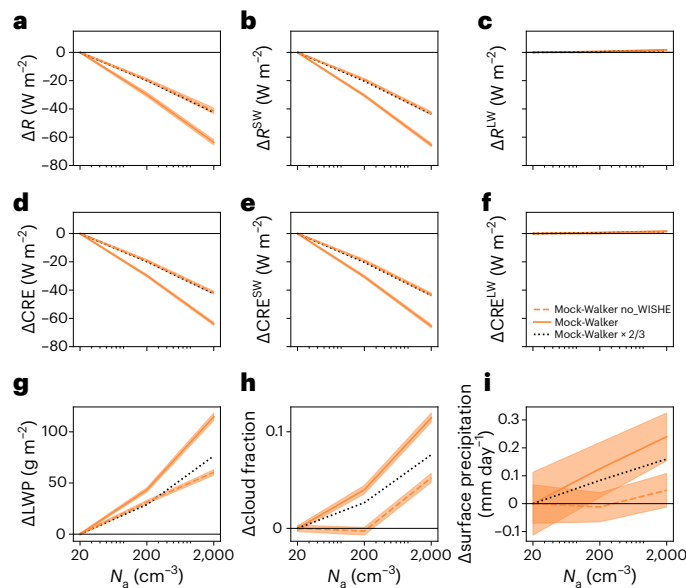
Fig. 6 | Mechanism denial experiment. a–c, The change in the net TOA energy gain (ΔR) in total (shortwave + longwave) (**a**), in the shortwave (**b**) and in the longwave (**c**). **d–f**, The change in the CRE in total (shortwave + longwave) (**d**), in the shortwave (**e**) and in the longwave (**f**). **g–i**, The change in the domain-mean LWP (including clear sky areas) (**g**), cloud fraction (**h**) and surface precipitation (**i**) owing to a change in aerosol concentration N_a (compared with the cleanest case of 20 cm^{-3}). This figure presents the results from the simulations conducted with and without WISHE (no_WISHE) feedback (see details in the text) and with SST of 300 K. The dashed black line represents two-thirds of the full trend seen in the mock-Walker simulation as reference. Solid lines represent domain-mean values, while shaded areas represent the 95th percentile uncertainty intervals ($n = 7,200$).

perturbations in the shallow and deep portions of the domain on the large-scale circulation adjustment, we conducted six additional simulations in which N_a is concentrated in either the high- or low-SST region (Methods and Supplementary Fig. 10). This set of simulations suggests

that addition of aerosol to the shallow-dominated regime indeed plays a larger role than addition of the same amount of aerosols to the deep regime (for more details see Supplementary Discussion 2), supporting our original hypothesis.

In this paper, we focus on 'adjustments' to ACI, that is, under a fixed SST framework. This framework's utility has been previously demonstrated, given that the atmospheric response operates on substantially shorter time scales compared with SST changes[5,10,33,34]. However, to verify the suitability of this separation in our own work, we need to make sure that the time required for the large-scale circulation adjustments to form is short compared with the time required for the SST to react substantially to the initial radiative forcing (on the order of a few years). In addition, we would like to estimate separately the relative importance of cloud adjustments from local ACI and cloud adjustments from large-scale circulation changes. To do this, we conducted four additional transient simulations branching off the mock-Walker simulation at different times and thus initiated with different initial conditions (Methods). These results (Supplementary Discussion 3) suggest that the vast majority of the cloud adjustments (the LWP and CF responses), and hence also a large fraction of the R^{SW} response, is driven by large-scale circulation adjustments rather than by local, faster reacting, adjustments. In addition, it demonstrates that the large-scale circulation adjustments occur on a time scale (on the order of a month) shorter than the time required for substantial SST changes (on the order of years).

Finally, to estimate the potential radiative effect of the proposed process chain in the real world, we multiply the $\frac{\partial R}{\partial \log N_a}$ estimated based on our simulations by $\Delta \log N_a$ derived from an observational-based data set[35] (Methods). Considering the full observed range of N_a, the total potential local (over the tropical Pacific) radiative effect is estimated to be −18.5 W m^{-2}. Considering only the 25th and 75th percentiles as the relevant N_a range (Supplementary Fig. 14), the estimated total potential local radiative effect is −5.5 W m^{-2}, still a substantial local radiative effect accounting for the local variability of N_a in the present day. However, it is important to mention that this signal is likely to be masked by other forms of variability occurring in the tropical Pacific on the relevant timescales (for example, the El Niño−Southern Oscillation cycle[36] and equatorial waves[37]).

Implications

The results presented here demonstrate that the coupling between clouds and the large-scale circulation amplifies the ERF_{ACI} through an intensification of the tropical overturning circulation. This study highlights the importance of considering the impacts of ACI on a broader spatial–temporal scale, and specifically suggests that possible variations in the large-scale circulation owing to an aerosol perturbation should be taken into account.

We propose that future research should address these issues by exploring the coupling of clouds and large-scale circulation under broad spatial–temporal scales, and by conducting dedicated global storm-resolving simulations[38]. While global storm-resolving simulations hold great promise for advancing our understanding of these complex interactions, the computational requirements for such simulations are still prohibitive. Therefore, our modelling setup, which includes representation of the large-scale circulation under equilibrium conditions while still resolving clouds in high temporal and spatial resolution, could serve as a bridge between the more traditional cloud-scale simulations used for ACI studies and global storm-resolving simulations.

A main finding of this paper is that a local and persistent (more than a month) aerosol perturbation in the subsiding region of the tropics could have a significant effect also downwind at the ascending region. This could have important implications for the possibility of future marine cloud brightening, that is, the deliberate enhancement of marine cloud reflectance by local injections of aerosol particles that serve as CCN[39]. Hence, these remote effects though large-scale circulation adjustments should be accounted for in any examination of such deliberate geoengineering activity.

In conclusion, our study contributes to a growing body of research that seeks to understand the complex interactions between aerosols, clouds and the large-scale circulation[10,25,40–43], with a specific focus on ACI. By identifying the importance of considering the impacts of ACI on a broader spatial–temporal scale, we hope to inspire further research and collaboration to advance our understanding of these crucial processes.

Online content

Any methods, additional references, Nature Portfolio reporting summaries, source data, extended data, supplementary information, acknowledgements, peer review information; details of author contributions and competing interests; and statements of data and code availability are available at https://doi.org/10.1038/s41561-023-01319-8.

References

1. Bellouin, N. et al. Bounding global aerosol radiative forcing of climate change. *Rev. Geophys.* **58**, e2019RG000660 (2020).
2. Twomey, S. Pollution and the planetary albedo. *Atmos. Environ.* **8**, 1251–1256 (1974).
3. Twomey, S. The influence of pollution on the shortwave albedo of clouds. *J. Atmos. Sci.* **34**, 1149–1152 (1977).
4. Albrecht, B. A. Aerosols, cloud microphysics, and fractional cloudiness. *Science* **245**, 1227–1230 (1989).
5. Sherwood, S. C. et al. Adjustments in the forcing-feedback framework for understanding climate change. *Bull. Am. Meteorol. Soc.* **96**, 217–228 (2015).
6. Wall, C. J. et al. Assessing effective radiative forcing from aerosol–cloud interactions over the global ocean. *Proc. Natl Acad. Sci. USA* **119**, 2210481119 (2022).
7. Watson-Parris, D. & Smith, C. J. Large uncertainty in future warming due to aerosol forcing. *Nat. Clim. Chang.* **12**, 1111–1113 (2022).
8. Gryspeerdt, E., Quaas, J. & Bellouin, N. Constraining the aerosol influence on cloud fraction. *J. Geophys. Res. Atmos.* **121**, 3566–3583 (2016).
9. Merlis, T. M. Direct weakening of tropical circulations from masked CO_2 radiative forcing. *Proc. Natl Acad. Sci. USA* **112**, 13167–13171 (2015).
10. Williams, A. I. L., Stier, P., Dagan, G. & Watson-Parris, D. Strong control of effective radiative forcing by the spatial pattern of absorbing aerosol. *Nat. Clim. Chang.* **12**, 735–742 (2022).
11. Bony, S. et al. Clouds, circulation and climate sensitivity. *Nat. Geosci.* **8**, 261–268 (2015).
12. Wing, A. A. & Cronin, T. W. Self-aggregation of convection in long channel geometry. *Q. J. R. Meteorol. Soc.* **142**, 1–15 (2016).
13. Cronin, T. W. & Wing, A. A. Clouds, circulation, and climate sensitivity in a radiative-convective equilibrium channel model. *J. Adv. Model. Earth Syst.* **9**, 2883–2905 (2017).
14. Wing, A. A. et al. Radiative–convective equilibrium model intercomparison project. *Geosci. Model Dev.* **11**, 793–813 (2018).
15. Wing, A. A. et al. Clouds and convective self-aggregation in a multimodel ensemble of radiative–convective equilibrium simulations. *J. Adv. Model. Earth Syst.* **12**, e2020MS002138 (2020).
16. Lutsko, N. & Cronin, T. W. Mean climate and circulation of mock-Walker simulations. In *Proc. 34th Conference on Hurricanes and Tropical Meteorology* (AMS, 2021).
17. Grabowski, W. W., Yano, J.-I. & Moncrieff, M. W. Cloud resolving modeling of tropical circulations driven by large-scale sst gradients. *J. Atmos. Sci.* **57**, 2022–2040 (2000).
18. Bretherton, C. S., Blossey, P. N. & Peters, M. E. Interpretation of simple and cloud-resolving simulations of moist convection–radiation interaction with a mock-Walker circulation. *Theor. Comput. Fluid Dyn.* **20**, 421–442 (2006).
19. van den Heever, S. C., Stephens, G. L. & Wood, N. B. Aerosol indirect effects on tropical convection characteristics under conditions of radiative–convective equilibrium. *J. Atmos. Sci.* **68**, 699–718 (2011).
20. Khairoutdinov, M. F. & Randall, D. A. Cloud resolving modeling of the arm summer 1997 IOP: model formulation, results, uncertainties, and sensitivities. *J. Atmos. Sci.* **60**, 607–625 (2003).
21. Wall, C. J., Storelvmo, T. & Possner, A. Global observations of aerosol indirect effects from marine liquid clouds. *Atmos. Chem. Phys.* **23**, 13125–13141 (2023).
22. Stevens, B. & Feingold, G. Untangling aerosol effects on clouds and precipitation in a buffered system. *Nature* **461**, 607–613 (2009).
23. Seifert, A., Heus, T., Pincus, R. & Stevens, B. Large-eddy simulation of the transient and near-equilibrium behavior of precipitating shallow convection. *J. Adv. Model. Earth Syst.* **7**, 1918–1937 (2015).
24. Dagan, G., Koren, I., Altaratz, O. & Heiblum, R. H. Aerosol effect on the evolution of the thermodynamic properties of warm convective cloud fields. *Sci. Rep.* **6**, 38769 (2016).
25. Dagan, G. Sub-tropical aerosols enhance tropical cloudiness—a remote aerosol-cloud lifetime effect. *J. Adv. Model. Earth Syst.* **14**, e2022MS003368 (2022).
26. Coppin, D. & Bony, S. Physical mechanisms controlling the initiation of convective self-aggregation in a general circulation model. *J. Adv. Model. Earth Syst.* **7**, 2060–2078 (2015).
27. Rosenfeld, D. et al. Flood or drought: how do aerosols affect precipitation? *Science* **321**, 1309–1313 (2008).
28. Fan, J., Wang, Y., Rosenfeld, D. & Liu, X. Review of aerosol–cloud interactions: mechanisms, significance, and challenges. *J. Atmos. Sci.* **73**, 4221–4252 (2016).
29. Chen, Q. et al. How do changes in warm-phase microphysics affect deep convective clouds? *Atmos. Chem. Phys.* **17**, 9585–9598 (2017).
30. Fan, J. et al. Microphysical effects determine macrophysical response for aerosol impacts on deep convective clouds. *Proc. Natl Acad. Sci. USA* **110**, 4581–4590 (2013).
31. Dagan, G. et al. Atmospheric energy budget response to idealized aerosol perturbation in tropical cloud systems. *Atmos. Chem. Phys.* **20**, 4523–4544 (2020).

32. Hartmann, D. L., Hendon, H. H. & Houze, R. A. Jr. Some implications of the mesoscale circulations in tropical cloud clusters for large-scale dynamics and climate. *J. Atmos. Sci.* **41**, 113–121 (1984).

33. Bony, S. et al. Robust direct effect of carbon dioxide on tropical circulation and regional precipitation. *Nat. Geosci.* **6**, 447–451 (2013).

34. Samset, B. H. et al. Fast and slow precipitation responses to individual climate forcers: a PDRMIP multimodel study. *Geophys. Res. Lett.* **43**, 2782–2791 (2016).

35. Choudhury, G. & Tesche, M. A first global height-resolved cloud condensation nuclei data set derived from spaceborne lidar measurements. *Earth Syst. Sci. Data* **15**, 3747–3760 (2023).

36. Ceppi, P. & Fueglistaler, S. The El Niño–Southern Oscillation pattern effect. *Geophys. Res. Lett.* **48**, e2021GL095261 (2021).

37. Wheeler, M. & Kiladis, G. N. Convectively coupled equatorial waves: analysis of clouds and temperature in the wavenumber–frequency domain. *J. Atmos. Sci.* **56**, 374–399 (1999).

38. Stevens, B. et al. DYAMOND: the DYnamics of the Atmospheric general circulation Modeled On Non-hydrostatic Domains. *Prog. Earth Planet. Sci.* **6**, 61 (2019).

39. Latham, J. et al. Marine cloud brightening. *Philos. Trans. R. Soc. A* **370**, 4217–4262 (2012).

40. Dagan, G. & Chemke, R. The effect of subtropical aerosol loading on equatorial precipitation. *Geophys. Res. Lett.* **43**, 11048–11056 (2016).

41. Johnson, B. T., Haywood, J. M. & Hawcroft, M. K. Are changes in atmospheric circulation important for black carbon aerosol impacts on clouds, precipitation, and radiation? *J. Geophys. Res. Atmos.* **124**, 7930–7950 (2019).

42. Richardson, T. B. et al. Efficacy of climate forcings in PDRMIP models. *J. Geophys. Res. Atmos.* **124**, 12824–12844 (2019).

43. Abbott, T. H. & Cronin, T. W. Aerosol invigoration of atmospheric convection through increases in humidity. *Science* **371**, 83–85 (2021).

Methods

Model description and experimental design

Version 6.11.7 of the SAM[20] is used here, together with a two-moment bulk microphysical scheme[44]. In the simulations presented here, we alter the CCN concentration (N_a, evaluated at 1% super-saturation) between three different, vertically uniform levels (20, 200 and 2,000 cm^{-3}), covering a large, but observationally plausible, range of conditions (Supplementary Fig. 14). The activation of CCN at the cloud base is parameterized following ref. 45. The Twomey effect[3] of both liquid and ice is considered. This is done by passing the cloud water and ice-crystal effective radii from the microphysical scheme to the radiation scheme. In these simulations, direct interactions between aerosols and radiation are not considered. Subgrid-scale fluxes are parameterized using Smagorinsky's eddy diffusivity model, and gravity waves are damped at the top of the domain. Concentrations of CO_2 are set at pre-industrial level (280 ppm). The O_3 vertical profile is similar to that in ref. 14 and represents a typical tropical atmosphere. Other trace gases (such as CH_4 and N_2O) are neglected for simplicity.

Following the Radiative–Convective Equilibrium Model Intercomparison Project (RCEMIP) protocol for the large-domain simulations (RCE_large)[14], the domain size is set to 6,144 × 384 km^2, with horizontal grid spacing of 3 km and doubly periodic boundary conditions. Sixty-four vertical levels are used in the mock-Walker simulations between 25 m and 27 km, with vertical grid spacing increasing from 50 m near the surface to roughly 1 km at the domain top. A time step of 12 s is used, and radiative fluxes are calculated every 5 min using the CAM radiation scheme[46]. The CRE is calculated by subtracting the clear-sky from the all-sky TOA radiative fluxes ($R - R_{clear-sky}$). The output resolution for all fields is 1 h. Following the RCEMIP protocol, a net insolation close to the tropical-mean value is set by fixing the incoming solar radiation at 551.58 W m^{-2}, with a zenith angle of 42.05°. A small thermal noise is added near the surface at the beginning of the simulation to initialize convection. The initial conditions for each simulation are based on the last 30 days of a 150-day-long small-domain RCE simulation for each SST (as described below). The simulations are conducted with an SST gradient along the long dimensions (X) of the domain (mock-Walker). The SST distribution is set as a sinusoidal function of X (Fig. 1). The SST range in this case is 5 K, which resembles the range observed over the tropical Pacific ocean[16].

In addition to the mock-Walker simulations, another set of simulations is conducted with homogeneous SST distribution (RCE_large, following the RCEMIP protocol) for comparison. In this case, we use 68 levels up to 31 km. Sensitivity tests demonstrate that the reduction in the number of vertical grid points in the mock-Walker simulations compared with the RCE_large simulations has no effect on the general conclusion of this paper. Up to the height of 27 km, the grid spacing is similar between the two sets of simulations (see more details about these two sets of simulation below).

For each set of simulations (RCE_large and mock-Walker), three domain-mean SSTs are considered: 295, 300 and 305 K. For each SST level and distribution, three simulations are conducted with the three different levels of N_a. That is, 18 baseline simulations are considered (two SST distributions × three domain-mean SSTs × three N_a concentrations), besides the mechanism denial, transient and non-uniform N_a simulations described below. The RCE_large simulations are integrated for 200 days. This is twice the time required in the RCEMIP protocol. The last 100 days of each simulation are used for the statistical analysis.

The mock-Walker simulations are integrated for 400 days, and the last 300 days of each simulation are used for the statistical analysis. In this case, a longer statistical sampling is needed, as in many of the simulations some of the domain-mean properties oscillate strongly with time with a few tens of days period (Supplementary Fig. 15). The reasons behind the oscillations deserve a separate study, but this does not significantly affect the domain-mean properties when averaged over 300 days. For example, the main conclusions of this paper do not

change if we base them on averages over the last 200 days rather than over the last 300 days of the simulations. The mock-Walker domains are divided to two parts dominated by shallow or deep convection. This deviation is done by two methods to assess the robustness of the results. The first method of division is based on the SST, with SST below the domain mean and above it referred to as the shallow and deep part, respectively (Fig. 1d, black vertical lines). The second method of division is based on the time-mean mid-troposphere vertical velocity (w_{500}), with $w_{500} > 0$ referred to as the deep part and $w_{500} < 0$ as the shallow part. We calculate the fluxes of water vapour and dry static energy out of the shallow- or deep-dominated regimes as $P - E$ and $L_vP + Q$, respectively, where P is the precipitation, E is the evaporation, L_v is the latent heat of vapourization and Q is the atmospheric diabatic heating due to radiative fluxes and surface sensible heat flux[47].

The 95% confidence intervals are presented in the different figures. In computing the confidence intervals, we accounted for serial correlation using 100 days for the maximum lag for autocovariance estimations (which is longer than the few tens of days variability; Supplementary Fig. 15). The results do not significantly change if we use 50 days instead.

Mechanism denial experiment

To examine the role of the enhanced surface wind speed in enhancing the surface evaporation and increasing the cloudiness, we conduct an additional set of mock-Walker simulations in which the surface wind speed is fixed at 3 m s^{-1} only for the surface fluxes calculation. This value was chosen as it represents the typical values observed in the shallow regime of the interactive surface fluxes simulations (Fig. 3j). We run these simulations for the three N_a concentrations considered here with SST of 300 K. This is done in order to 'turn off' the feedback between N_a and surface evaporation, to evaluate its role. Here again, the simulations are integrated for 400 days and the last 300 days are used for the statistical analysis. Examining the distribution of cloud top height between the baseline ($N_a = 20$ cm^{-3}) mechanism denial simulation and the regular simulation demonstrates that there are no significant differences in the cloud regime distribution (Supplementary Fig. 16). Hence, differences between these simulations cannot be explained solely by a shift in the cloud regimes.

Transient simulations

To estimate the relative importance of cloud adjustments from local ACI and cloud adjustments from large-scale circulation changes, and to evaluate the time required for the large-scale circulation adjustments, we conducted four additional 100-day-long transient simulations branching off the mock-Walker simulation conducted with SST of 300 K and N_a of 20 cm^{-3} at different times (after 100, 200, 300 and 400 days of the original simulation). These transient simulations were conducted with a higher N_a of 2,000 cm^{-3} to maximize the response. As these four different simulations were initiated with different initial conditions but after the spin-up of the first 100 days, they allow evaluation of the transient response of the circulation and clouds to the aerosol perturbation. We note that four ensemble members are not sufficient to cover the entire spectrum of possible initial conditions and do not eliminate completely the role of internal variability. However, the fact that the ensemble-mean difference stabilizes during the last 50 days of the simulation at around the difference seen in the original, longer (400 days), runs, gives us confidence in its ability to capture the main trends.

Non-spatially uniform N_a simulations

To evaluate the relative importance of the aerosol effect on deep and shallow clouds on the large-scale circulation adjustments, we conducted six additional 400-day-long simulations in which N_a is not spatially uniform but concentrated in the high- or low-SST region (referred to as deep and shallow concentrated pollution, or in short Deep_POL and

Shallow_POL, respectively). This is done by applying an N_a distribution along the x axis which resembles, or has an opposite phase to, the SST distribution (Supplementary Fig. 10). Each N_a distribution was used under the three different domain-mean SSTs.

N_a observations

We use an observational-based data set of N_a (ref. 35). Our results indicate that aerosol loading in the subsiding region of the tropical Pacific is key for the large-scale circulation adjustments and that the aerosol perturbation should last for at least a month for the large-scale circulation adjustments to take place. Hence, we focus on monthly variations of $\log N_a$ over the subsiding region of the tropical Pacific ($-10°$ to $10°$ N, $80°$ to $130°$ W; Supplementary Fig. 14). The N_a data set spans 15.5 years in which the total range of monthly mean N_a in the boundary layer in our region of interest is $230-1,260\,cm^{-3}$.

Data availability

The data presented in this study are publicly available at https://zenodo.org/record/7707639.

Code availability

SAM is publicly available at http://rossby.msrc.sunysb.edu/~marat/SAM/.

References

44. Morrison, H., Curry, J. A. & Khvorostyanov, V. I. A new double-moment microphysics parameterization for application in cloud and climate models. Part I: description. *J. Atmos. Sci.* **62**, 1665–1677 (2005).

45. Twomey, S. The nuclei of natural cloud formation part II: the supersaturation in natural clouds and the variation of cloud droplet concentration. *Geofisica pura e applicata* **43**, 243–249 (1959).

46. Collins, W. D. et al. The formulation and atmospheric simulation of the community atmosphere model version 3 (CAM3). *J. Climate* **19**, 2144–2161 (2006).

47. Dagan, G., Stier, P., Dingley, B. & Williams, A. I. L. Examining the regional co-variability of the atmospheric water and energy imbalances in different model configurations—linking clouds and circulation. *J. Adv. Model. Earth Syst.* **14**, e2021MS002951 (2022).

Author contributions

G.D. conducted the simulations, performed the analysis and wrote the initial manuscript draft. N.Y. and A.I.L.W. contributed to the design of the study, interpretation of the results and improvement of the manuscript.

Competing interests

The authors declare no competing interests.

Additional information

Supplementary information The online version contains supplementary material available at https://doi.org/10.1038/s41561-023-01319-8.

Correspondence and requests for materials should be addressed to Guy Dagan.

Peer review information *Nature Geoscience* thanks the anonymous reviewers for their contribution to the peer review of this work. Primary Handling Editor: Tom Richardson, in collaboration with the *Nature Geoscience* team.

Reprints and permissions information is available at www.nature.com/reprints.